ELSEVIER

Comput. Methods Appl. Mech. Engrg. 190 (2001) 5639–5656

Computer methods in applied mechanics and engineering

www.elsevier.com/locate/cma

A method of substructuring large-scale computational micromechanical problems

T.I. Zohdi [a,*], P. Wriggers [a], C. Huet [b]

[a] Institut für Baumechanik und Numerische Mechanik, Universitat Hannover, Appelstrasse 9A, D-30167 Hannover, Germany

[b] Laboratoire de Matériaux de Construction, Département des Matériaux, Ecole Polytechnique Fédérale de Lausanne, CH-1015 Lausanne EPFL, Switzerland

Received 4 August 2000; accepted 31 January 2001

Abstract

In this work, a method is developed to decompose or *substructure* large-scale micromechanical simulations into a set of computationally smaller problems. In the approach the global domain is partitioned into nonoverlapping subdomains. On the interior subdomain partitions an approximate globally kinematically admissible solution is projected. This allows the subdomains to be mutually decoupled, and therefore separately solvable. The subdomain boundary value problems are solved with the exact microstructural representation contained within their respective boundaries, but with approximate displacement boundary data. The resulting microstructural solution is the assembly of the subdomain solutions, each restricted to its corresponding subdomain. The approximate solution is far more inexpensive to compute than the direct problem. A posteriori error bounds are developed to quantify the quality of the approximate solution. Numerical simulations are presented to illustrate the essential concepts.

Keywords: Micromechanics; Large-scale computing; Substructuring

1. Introduction

In many emerging technologies knowledge of microscopic fields, such as mechanical stress fields, diffusive fields, thermal fields, etc., within mesoscale structural components ($\approx$0.0001–0.01 m) are desired. For example, such information may be needed to estimate a miniature computer component's useful service life. However, difficulties arise in the numerical simulation of such problems, which possess irregular fine scale heterogeneous microstructure. This is due to the fact that the spatial discretization mesh size must be smaller than the intrinsic micromechanical length scales for reasonable accuracy. This results in immense memory requirements to store the algebraic systems, and a correspondingly large number of floating point operations to solve them. For example, in materials having particulate microstructure, a cube of dimensions 0.0001 m $\times$ 0.0001 m $\times$ 0.0001 m can typically contain on the order of 1000–10,000 particles suspended in a binding matrix (Fig. 1). Typically, for three-dimensional problems, in the range of 1000–5000 numerical degrees of freedom per particle are needed to deliver numerically accurate solutions. Therefore, a detailed boundary value representation, i.e., employing the microstructural geometry, is computationally expensive to solve due to the highly heterogeneous microstructure.

* Corresponding author. Present address: Department of Mechanical Engineering, 6195 Etcheverry Hall, The University of California, Berkeley, CA 94720-1740, USA. Tel.: +1-510-642-6834; fax: +1-510-642-6163.

E-mail addresses: zohdi@newton.berkeley.edu (T.I. Zohdi), wriggers@ibnm.uni-hannover.de (P. Wriggers), christian.huet@epfl.ch (C. Huet).

0045-7825/01/$ - see front matter
PII: S0045-7825(01)00189-X

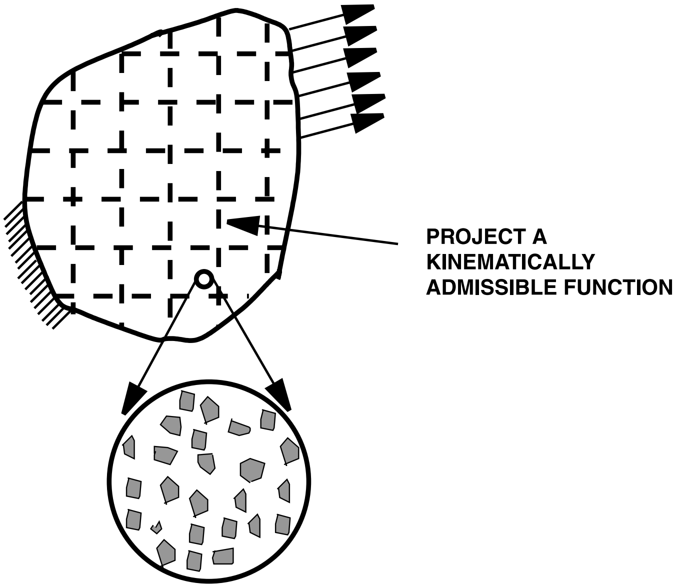

Fig. 1. Construction of the approximate solution.

In an attempt to reduce computational effort, we consider a set of 'broken' nonoverlapping subdomain boundary value problems whose (sub)domains' union form the entire domain under analysis (Fig. 1). The subdomain boundary value problems have the exact microstructural representation contained within the subdomain, but approximate displacement boundary data. The approximate global microstructural solution is the assembly of the subdomain solutions, each restricted to its corresponding subdomain. For example, if one considers a cubical domain, whose response is simulated using n numerical unknowns, for example, employing a finite element discretization, approximately $\mathrm{O}(n^{\gamma})$ floating point operations are needed to solve the system. The value of γ, typically $2 \leqslant \gamma \leqslant 3$, depends on the type of algebraic system solver used. If the cube was divided into N equal subdomains (subcubes), the number of floating point operations needed would be approximately on the order of $(n/N)^{\gamma}N$, and thus *direct costs/decomposed costs* $\approx N^{\gamma-1}$. For example, if one had 1000 subdomains, the broken solution costs between 1000 and 1,000,000 times less to compute than the globally exact solution. The advantages are not limited to the possible reduction of operation counts, since the subdomain problems can be solved separately, and trivially in parallel. If parallel processing is used for the decomposed problem, which by construction has a perfect speedup, then the ratio of costs becomes $PN^{\gamma-1}$, where P denotes the number of processors. However, the reduction of costs are not for free, since there is a partitioning error involved. The characterization of such error is a main component of the work to be presented.

The outline of the presentation is as follows. In Section 2, the governing equations are laid down for the so-called broken problems. In Section 3, the error in the process is characterized in terms of a potential, and thereafter error bounds are developed. In Section 4, a large-scale numerical example is given. In Section 5, the effects of numerical discretization are discussed. In Section 6, extensions, namely, iterative procedures to deliver solutions of arbitrarily low error, are discussed.

2. Governing equations

We consider a structure which occupies an open bounded domain in $\Omega \in \mathbb{R}^3$. Its boundary is denoted $\partial\Omega$. The body is in static equilibrium under the action of body forces, $\boldsymbol{f}$, and surface tractions, $\boldsymbol{t}$. The boundary $\overline{\partial\Omega} = \overline{\Gamma_u \cup \Gamma_t}$ consists of a part Γ_u and a part Γ_t on which displacements and tractions are, respectively, prescribed. The data are assumed to be such that $\boldsymbol{f} \in \boldsymbol{L}^2(\Omega)$ and $\boldsymbol{t} \in \boldsymbol{L}^2(\Gamma_t)$, but less smooth data can be considered without complications. The mechanical properties of the material are characterized by the elasticity tensor, $\mathbb{E} \in \mathbb{R}^{3^2 \times 3^2}$, whose components are functions of spatial position in the body, and which satisfy the following symmetry and boundedness conditions, $\alpha_+ \boldsymbol{\epsilon} : \boldsymbol{\epsilon} \geqslant \boldsymbol{\epsilon} : \mathbb{E}(\boldsymbol{x}) : \boldsymbol{\epsilon} \geqslant \alpha_- \boldsymbol{\epsilon} : \boldsymbol{\epsilon} \forall \boldsymbol{\epsilon} \in \mathbb{R}^{3\times 3}$, $\boldsymbol{\epsilon} = \boldsymbol{\epsilon}^{\mathrm{T}}$, $\infty > \alpha_+, \alpha_- > 0$, $E_{ijkl}(\boldsymbol{x}) = E_{jikl}(\boldsymbol{x}) = E_{ijlk}(\boldsymbol{x}) = E_{klij}(\boldsymbol{x})$, $1 \leqslant i,j,k,l \leqslant 3$, $E_{ijkl}(\boldsymbol{x})$ being the Cartesian components of $\mathbb{E}$ at point $\boldsymbol{x}$. The microstructure is assumed to be perfectly bonded. Throughout the analysis we use $H^1(\Omega)$ to denote the usual space of functions with generalized partial derivatives of order $\leqslant 1$ in $L^2(\Omega)$. We define $\boldsymbol{H}^1(\Omega) \stackrel{\text{def}}{=} [H^1(\Omega)]^3$ as the (Sobolev) space of vector-valued functions whose components are in $H^1(\Omega)$. Throughout this work, we shall use the symbol '$\boldsymbol{u}|_{\partial\Omega}$' for boundary values.

2.1. Boundary value problem formulations

The globally exact solution, $\boldsymbol{u}$, is characterized by the following virtual work formulation:

$$\boxed{\begin{array}{l}\text{Find } \boldsymbol{u} \in \boldsymbol{H}^1(\Omega),\ \ \boldsymbol{u}|_{\Gamma_u} = \boldsymbol{d}, \quad \text{such that} \\ \displaystyle\int_\Omega \nabla \boldsymbol{v} :\ \boldsymbol{\sigma}\, \mathrm{d}\Omega = \int_\Omega \boldsymbol{f} \cdot \boldsymbol{v}\, \mathrm{d}\Omega + \int_{\Gamma_t} \boldsymbol{t} \cdot \boldsymbol{v}\, \mathrm{d}A \quad \forall \boldsymbol{v} \in \boldsymbol{H}^1(\Omega),\ \ \boldsymbol{v}|_{\Gamma_u} = \mathbf{0},\end{array}} \tag{1}$$

where $\boldsymbol{\sigma}$ is the Cauchy stress. In the infinitesimal strain, linearly elastic, case $\boldsymbol{\sigma} = \mathbb{E} : \nabla \boldsymbol{u}$. In order to construct approximate solutions, next we consider the subdomain boundary value problems, which have the exact microstructural representation contained within the domain, but approximate *displacement* boundary data on the interior subdomain boundaries.

To construct the approximate microstructural solutions we first partition the domain, Ω, into N nonintersecting open subdomains $\bigcup_{K=1}^{N} \Omega_K = \overline{\Omega}$. We define the boundary of an individual subdomain Ω_K, as $\partial\Omega_K$. When employing the applied internal displacement approach, a kinematically admissible function, $\boldsymbol{U} \in \boldsymbol{H}^1(\Omega)$ and $\boldsymbol{U}|_{\Gamma_u} = \boldsymbol{d}$, is projected onto the *internal boundaries* of the subdomain partitions. Any subdomain boundaries coinciding with the exterior surface retain their original boundary conditions (Fig. 1). Accordingly, we have the following virtual work formulation, for each subdomain, $1 \leqslant K \leqslant N$:

$$\boxed{\begin{array}{l}\text{Find } \tilde{\boldsymbol{u}}_K \in \boldsymbol{H}^1(\Omega_K),\ \ \tilde{\boldsymbol{u}}_K|_{\partial\Omega_K \cap (\Omega \cup \Gamma_u)} = \boldsymbol{U} \in \boldsymbol{H}^1(\Omega), \quad \text{such that} \\ \displaystyle\int_{\Omega_K} \nabla \boldsymbol{v}_K :\ \tilde{\boldsymbol{\sigma}}_K\, \mathrm{d}\Omega = \int_{\Omega_K} \boldsymbol{f} \cdot \boldsymbol{v}_K\, \mathrm{d}\Omega + \int_{\partial\Omega_K \cap \Gamma_t} \boldsymbol{t} \cdot \boldsymbol{v}_K\, \mathrm{d}A \\ \qquad \forall \boldsymbol{v}_K \in \boldsymbol{H}^1(\Omega_K),\ \ \boldsymbol{v}_K|_{\partial\Omega_K \cap (\Omega \cup \Gamma_u)} = \mathbf{0}.\end{array}} \tag{2}$$

The constitutive law and microstructure are identical to that of the globally exact problem. In the infinitesimal strain, linearly elastic, case $\tilde{\boldsymbol{\sigma}} = \mathbb{E} : \nabla \tilde{\boldsymbol{u}}_K$. The individual subdomain solutions, $\tilde{\boldsymbol{u}}_K$, are 0 outside of the corresponding subdomain $\overline{\Omega}_K$. In this case the approximate solution is constructed by a direct assembly process

$$\boxed{\tilde{\boldsymbol{u}} \stackrel{\text{def}}{=} \boldsymbol{U} + (\tilde{\boldsymbol{u}}_1 - \boldsymbol{U})|_{\Omega_1} + (\tilde{\boldsymbol{u}}_2 - \boldsymbol{U})|_{\Omega_2} + \cdots + (\tilde{\boldsymbol{u}}_N - \boldsymbol{U})|_{\Omega_N}.} \tag{3}$$

The approximate displacement field is in $\boldsymbol{H}^1(\Omega)$, however, the approximate traction field is possibly discontinuous. Logical choices of $\boldsymbol{U}$ will be given later in the work. It should be clear that if $\boldsymbol{U} = \boldsymbol{u}$ on the internal partition boundaries, then the approximate solution is exact.

Remark. In theory, an approach of projecting the tractions could be developed. However, such an approach has a number of difficulties, in particular the pure traction subdomain problems must have equilibrated tractions to be well posed. To impose this on the numerical implementation level is not a trivial task. Primarily for this reason the projected displacement approach is preferable.

3. Error in the broken problems

Since we employ energy-type variational principles to generate approximate solutions, we use energy-type measures for the error. Directly by the use of the divergence theorem one has

$$\boxed{\begin{aligned}\int_\Omega \nabla(\boldsymbol{u}-\tilde{\boldsymbol{u}}) : (\boldsymbol{\sigma}-\tilde{\boldsymbol{\sigma}})\,\mathrm{d}\Omega &= \sum_{K=1}^{N}\int_{\Omega_K}\nabla(\boldsymbol{u}-\tilde{\boldsymbol{u}}_K) : (\boldsymbol{\sigma}-\tilde{\boldsymbol{\sigma}}_K)\,\mathrm{d}\Omega_K \\ &= \sum_{K=1}^{N}\int_{\Omega_K}\nabla\cdot((\boldsymbol{u}-\tilde{\boldsymbol{u}}_K)\cdot(\boldsymbol{\sigma}-\tilde{\boldsymbol{\sigma}}_K))\,\mathrm{d}\Omega_K \\ &\quad -\sum_{K=1}^{N}\int_{\Omega_K}(\boldsymbol{u}-\tilde{\boldsymbol{u}}_K)\cdot\underbrace{\nabla\cdot(\boldsymbol{\sigma}-\tilde{\boldsymbol{\sigma}}_K)}_{=\mathbf{0}}\,\mathrm{d}\Omega_K \\ &= \sum_{K=1}^{N}\int_{\partial\Omega_K\cap\Omega}\underbrace{(\tilde{\boldsymbol{\sigma}}_K\cdot\boldsymbol{n}_K)}_{\text{not continuous}}\cdot\underbrace{(\tilde{\boldsymbol{u}}_K-\boldsymbol{u})}_{\text{error}}\,\mathrm{d}A_K \\ &= \sum_{\mathscr{I}=1}^{N_{\mathscr{I}}}\int_{\Gamma_{\mathscr{I}}}(\text{traction jump})\cdot(\text{displacement error})\,\mathrm{d}A_K,\end{aligned}} \tag{4}$$

where $\Gamma_{\mathscr{I}}$ is an interior subdomain interface, and $\mathscr{I}=1,2,\ldots,N_{\mathscr{I}}=$ number of interior subdomain interfaces. For the applied internal displacement case, the tractions may suffer discontinuities at the interior subdomain boundaries (see Fig. 2). In the case of infinitesimal strain, linear elasticity, we have

$$\boxed{\begin{aligned}&\|\boldsymbol{u}-\tilde{\boldsymbol{u}}\|^2_{E(\Omega)} = \sum_{K=1}^{N}\int_{\partial\Omega_K\cap\Omega}\underbrace{(\mathbb{E} : \nabla\tilde{\boldsymbol{u}}_K\cdot\boldsymbol{n}_K)}_{\text{not continuous}}\cdot\underbrace{(\tilde{\boldsymbol{u}}_K-\boldsymbol{u})}_{\text{error}}\,\mathrm{d}A_K, \\ &\|\boldsymbol{u}-\tilde{\boldsymbol{u}}\|^2_{E(\Omega)} \stackrel{\text{def}}{=} \int_\Omega\nabla(\boldsymbol{u}-\tilde{\boldsymbol{u}}) : \mathbb{E} : \nabla(\boldsymbol{u}-\tilde{\boldsymbol{u}})\,\mathrm{d}\Omega.\end{aligned}} \tag{5}$$

It is convenient to cast the error in terms of the potential energy for the case of linear elasticity,

$$\mathscr{J}(\boldsymbol{w}) \stackrel{\text{def}}{=} \frac{1}{2}\int_\Omega\nabla\boldsymbol{w} : \mathbb{E} : \nabla\boldsymbol{w}\,\mathrm{d}\Omega - \int_\Omega\boldsymbol{f}\cdot\boldsymbol{w}\,\mathrm{d}\Omega - \int_{\Gamma_t}\boldsymbol{t}\cdot\boldsymbol{w}\,\mathrm{d}A,$$

where $\boldsymbol{w}$ is any kinematically admissible function. The well-known relationship for any kinematically admissible function $\boldsymbol{w}$ is

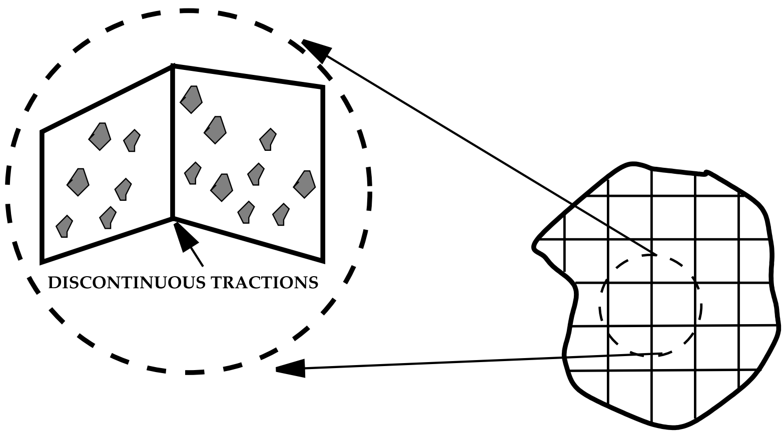

Fig. 2. The consequences of the projection approach.

$$\|\boldsymbol{u}-\boldsymbol{w}\|^2_{E(\Omega)} = 2(\mathscr{J}(\boldsymbol{w})-\mathscr{J}(\boldsymbol{u})) \quad \text{or} \quad \mathscr{J}(\boldsymbol{u}) \leqslant \mathscr{J}(\boldsymbol{w}), \tag{6}$$

which is the principle of minimum potential energy (PMPE). In other words, the true solution possesses a minimum potential. Therefore, since $\tilde{\boldsymbol{u}}$ is kinematically admissible, we immediately have $\|\boldsymbol{u}-\tilde{\boldsymbol{u}}\|^2_{E(\Omega)} = 2(\mathscr{J}(\tilde{\boldsymbol{u}})-\mathscr{J}(\boldsymbol{u}))$. The critical observation is that if we can bound $\mathscr{J}(\boldsymbol{u})$ from below, then we can bound the error from above. In other words, what we seek is $\mathscr{J}^- \leqslant \mathscr{J}(\boldsymbol{u})$.

To bound $\mathscr{J}(\boldsymbol{u})$ in terms of easily accessible quantities, we first calculate a computationally inexpensive, kinematically admissible, regularized test solution. The regularized test solution, $\boldsymbol{u}^{\mathrm{R}}$, is characterized by a virtual work formulation:

$$\boxed{\begin{array}{l}\text{Find } \boldsymbol{u}^{\mathrm{R}} \in \boldsymbol{H}^1(\Omega),\ \boldsymbol{u}^{\mathrm{R}}|_{\Gamma_u} = \boldsymbol{d}, \quad \text{such that} \\ \quad \displaystyle\int_\Omega \nabla \boldsymbol{v} : \boldsymbol{\sigma}^{\mathrm{R}}\,\mathrm{d}\Omega = \int_\Omega \boldsymbol{f}\cdot\boldsymbol{v}\,\mathrm{d}\Omega + \int_{\Gamma_t} \boldsymbol{t}\cdot\boldsymbol{v}\,\mathrm{d}A \quad \forall \boldsymbol{v} \in \boldsymbol{H}^1(\Omega), \boldsymbol{v}|_{\Gamma_u} = \boldsymbol{0}.\end{array}} \tag{7}$$

Here the constitutive law for $\boldsymbol{\sigma}^{\mathrm{R}}$ should be taken to be as simple as a possible, i.e., a constant (regularized) fourth-order symmetric positive definite linear elasticity tensor $\mathscr{R}$, defined via $\boldsymbol{\sigma}^{\mathrm{R}} = \mathscr{R} : \nabla \boldsymbol{u}^{\mathrm{R}}$. *In general, the regularized solution* $(\boldsymbol{\sigma}^{\mathrm{R}}, \boldsymbol{u}^{\mathrm{R}})$ *does not coincide with the field associated with the decoupling solution* $\boldsymbol{U}$. If we choose $\boldsymbol{w} = \boldsymbol{u}^{\mathrm{R}}$ in Eq. (6), which is an admissible function, we obtain $\|\boldsymbol{u}-\boldsymbol{u}^{\mathrm{R}}\|^2_{E(\Omega)} = 2(\mathscr{J}(\boldsymbol{u}^{\mathrm{R}})-\mathscr{J}(\boldsymbol{u}))$, which implies $\mathscr{J}(\boldsymbol{u}) = \mathscr{J}(\boldsymbol{u}^{\mathrm{R}}) - \frac{1}{2}\|\boldsymbol{u}-\boldsymbol{u}^{\mathrm{R}}\|^2_{E(\Omega)}$. Our objective is to form an *upper bound* on $\|\boldsymbol{u}-\boldsymbol{u}^{\mathrm{R}}\|_{E(\Omega)}$ in terms of $\mathscr{R}$, $\mathbb{E}$ and $\nabla\boldsymbol{u}^{\mathrm{R}}$, to obtain a *lower bound* on $\mathscr{J}(\boldsymbol{u})$. For the bound to be useful, it should contain no unknown constants, and should be solely in terms of the regularized solution and the material data. In other words we seek $\|\boldsymbol{u}-\boldsymbol{u}^{\mathrm{R}}\|_{E(\Omega)} \leqslant \mathscr{H}^+$, which will lead to $\mathscr{J}^- \stackrel{\text{def}}{=} \mathscr{J}(\boldsymbol{u}^{\mathrm{R}}) - \frac{1}{2}(\mathscr{H}^+)^2 \leqslant \mathscr{J}(\boldsymbol{u})$, thus supplying an upper bound for the quantities in Box (5).

By definition

$$\int_\Omega \nabla\boldsymbol{v} : \mathbb{E} : \nabla\boldsymbol{u}\,\mathrm{d}\Omega = \int_\Omega \nabla\boldsymbol{v} : \mathscr{R} : \nabla\boldsymbol{u}^{\mathrm{R}}\,\mathrm{d}\Omega = \int_\Omega \boldsymbol{f}\cdot\boldsymbol{v}\,\mathrm{d}\Omega + \int_{\Gamma_t}\boldsymbol{t}\cdot\boldsymbol{v}\,\mathrm{d}A, \tag{8}$$

and subtracting $\int_\Omega \nabla\boldsymbol{v} : \mathbb{E} : \nabla\boldsymbol{u}^{\mathrm{R}}\,\mathrm{d}\Omega$ from both sides yields

$$\int_\Omega \nabla\boldsymbol{v} : \mathbb{E} : \nabla\big(\boldsymbol{u}-\boldsymbol{u}^{\mathrm{R}}\big)\,\mathrm{d}\Omega = \int_\Omega \nabla\boldsymbol{v} : \big(\mathscr{R} : \nabla\boldsymbol{u}^{\mathrm{R}} - \mathbb{E} : \nabla\boldsymbol{u}^{\mathrm{R}}\big)\,\mathrm{d}\Omega. \tag{9}$$

Since $\boldsymbol{v}$ is an arbitrary virtual displacement, we may set $\boldsymbol{v} = \boldsymbol{u}-\boldsymbol{u}^{\mathrm{R}}$ in Eq. (9) to yield

$$\begin{aligned}\|\boldsymbol{u}-\boldsymbol{u}^{\mathrm{R}}\|^2_{E(\Omega)} &= \int_\Omega \nabla\big(\boldsymbol{u}-\boldsymbol{u}^{\mathrm{R}}\big) : \big(\mathscr{R} : \nabla\boldsymbol{u}^{\mathrm{R}} - \mathbb{E} : \nabla\boldsymbol{u}^{\mathrm{R}}\big)\,\mathrm{d}\Omega \\ &= \int_\Omega \mathbb{E}^{1/2} : \nabla\big(\boldsymbol{u}-\boldsymbol{u}^{\mathrm{R}}\big) : \mathbb{E}^{1/2} : \mathbb{E}^{-1} : \big(\mathscr{R} : \nabla\boldsymbol{u}^{\mathrm{R}} - \mathbb{E} : \nabla\boldsymbol{u}^{\mathrm{R}}\big)\,\mathrm{d}\Omega \\ &\leqslant \underbrace{\left(\int_\Omega \nabla\big(\boldsymbol{u}-\boldsymbol{u}^{\mathrm{R}}\big) : \mathbb{E} : \nabla\big(\boldsymbol{u}-\boldsymbol{u}^{\mathrm{R}}\big)\,\mathrm{d}\Omega\right)^{1/2}}_{\|\boldsymbol{u}-\boldsymbol{u}^{\mathrm{R}}\|_{E(\Omega)}} \\ &\quad \times \left(\int_\Omega \big(\mathscr{R} : \nabla\boldsymbol{u}^{\mathrm{R}} - \mathbb{E} : \nabla\boldsymbol{u}^{\mathrm{R}}\big) : \mathbb{E}^{-1} : \big(\mathscr{R} : \nabla\boldsymbol{u}^{\mathrm{R}} - \mathbb{E} : \nabla\boldsymbol{u}^{\mathrm{R}}\big)\,\mathrm{d}\Omega\right)^{1/2}.\end{aligned} \tag{10}$$

Therefore,

$$\boxed{\|\boldsymbol{u}-\boldsymbol{u}^{\mathrm{R}}\|^2_{E(\Omega)} \leqslant \textstyle\int_\Omega ((\mathbb{E}-\mathscr{R}) : \nabla\boldsymbol{u}^{\mathrm{R}}) : \mathbb{E}^{-1} : ((\mathbb{E}-\mathscr{R}) : \nabla\boldsymbol{u}^{\mathrm{R}})\,\mathrm{d}\Omega \stackrel{\text{def}}{=} \mathscr{H}^{+^2}.} \tag{11}$$

To derive this result we used the fact that a symmetric positive definite matrix has a unique positive square root, $\mathbb{E} = \mathbb{E}^{1/2} : \mathbb{E}^{1/2}$ and the Cauchy–Schwarz inequality. Note that the $\mathscr{H}^+$-bound depends only on $\mathscr{R}$, $\mathbb{E}$ and $\nabla\boldsymbol{u}^{\mathrm{R}}$. Therefore, using Box (11) we have $\mathscr{J}^- \stackrel{\text{def}}{=} \mathscr{J}(\boldsymbol{u}^{\mathrm{R}}) - \frac{1}{2}(\mathscr{H}^+)^2 \leqslant \mathscr{J}(\boldsymbol{u})$, and thus

$$\boxed{\underbrace{\|\boldsymbol{u}-\tilde{\boldsymbol{u}}\|^2_{E(\Omega)}}_{\text{error}=2(\mathscr{J}(\tilde{\boldsymbol{u}})-\mathscr{J}(\boldsymbol{u}))} \leqslant \underbrace{2(\mathscr{J}(\tilde{\boldsymbol{u}})-\mathscr{J}^-)}_{\text{upper bound}}.} \tag{12}$$

Remarks.

1. Bounds of such type have been studied in [8–10], however, they required that the decoupling solution $\boldsymbol{U}$ be identical to $\boldsymbol{u}^{\mathrm{R}}$. *Clearly this is unnecessary*. In the preceding bound, the tensor $\mathscr{R}$ did not have to be constant, and this has been exploited to generate hierarchical micromechanical models in [9]. More general theoretical aspects of such bounds, including their complementary (dual) formulation counterparts, can be found in [10,12]. Under certain conditions, such bounds coincide with results found in [4,5].
2. It is important to realize that the only approximation in this entire estimate is $\|\boldsymbol{u}-\boldsymbol{u}^{\mathrm{R}}\|_{E(\Omega)} \leqslant \mathscr{H}^+$. Thus, the ratio

$$\varrho \stackrel{\text{def}}{=} \frac{\mathscr{H}^+}{\|\boldsymbol{u}-\boldsymbol{u}^{\mathrm{R}}\|_{E(\Omega)}}$$

is an extremely good indicator of the quality of the estimate. Numerical and theoretical studies of the proximity of ϱ to unity has been studied in [8–12]. It is clear that the tensorial parameter $\mathscr{R}$ is free to choose, provided it is symmetric and positive definite. Thus, ideally, one would want to minimize $\varrho - 1$, in other words

$$\frac{\partial(\varrho-1)}{\partial\mathscr{R}} = \boldsymbol{0}, \qquad \frac{\partial^2(\varrho-1)}{\partial\mathscr{R}^2} > \boldsymbol{0} \;\Rightarrow\; \mathscr{R}^*.$$

Unfortunately, minimization of $\varrho - 1$ *is usually impossible, since* $\|\boldsymbol{u}-\boldsymbol{u}^{\mathrm{R}}\|_{E(\Omega)}$ *is unknown*. However, another avenue to optimize the bound is possible. Formally, the process to obtain the optimal choice, $\mathscr{R}^*$, *is to maximize the lower bound* $\mathscr{J}^-$, in other words

$$\frac{\partial\mathscr{J}^-}{\partial\mathscr{R}} = \boldsymbol{0}, \qquad \frac{\partial^2\mathscr{J}^-}{\partial\mathscr{R}^2} < \boldsymbol{0} \;\Rightarrow\; \mathscr{R}^*.$$

For example, if we consider a one-dimensional displacement controlled structure

$$\boxed{0 < x < L: \; \frac{\mathrm{d}}{\mathrm{d}x}\left(E(x)\frac{\mathrm{d}u}{\mathrm{d}x}\right) = 0, \quad u(0) = \varDelta_0, \;\; u(L) = \varDelta_L,} \tag{13}$$

it is easy to show that

$$\boxed{\varrho = \frac{\mathscr{H}^+}{\|u-u^{\mathrm{R}}\|_{E(\Omega)}} = \sqrt{\frac{\int_0^1\left(\frac{1}{\mathsf{R}}-\frac{1}{E}\right)^2 E\,\mathrm{d}x}{\int_0^1\left(\frac{1}{\mathsf{R}}-\frac{1}{E}\beta\right)^2 E\,\mathrm{d}x}}, \quad \beta \stackrel{\text{def}}{=} \frac{\left\langle\frac{1}{\mathsf{R}}\right\rangle_L}{\left\langle\frac{1}{E}\right\rangle_L},} \tag{14}$$

where the estimate is exact ($\varrho = 1$) for

$$\mathsf{R} = \left\langle\frac{1}{E}\right\rangle_L^{-1} \stackrel{\text{def}}{=} \left(\frac{1}{L}\int_0^L \frac{1}{E}\,\mathrm{d}x\right)^{-1}.$$

This value of R *also maximizes* $\mathscr{J}^-$. We remark that for traction controlled loading $u(0) = 0$, $E(\mathrm{d}u/\mathrm{d}x)(L) = G$, for a given G, the error estimate is exact for any R. For three-dimensional problems, the optimal tensor $\mathscr{R}^*$, which is problem dependent, is easily computable, since it requires *no* microscale computations.

4. A numerical example

As an example, we apply the decomposition approach to a sample of material containing a significant amount of microstructure (Fig. 3). We simulated a rectangular block composed of an aluminum matrix ($(\kappa, \mu) = (77.9, 24.9)$ GPa), containing 10,240 boron particles ($(\kappa, \mu) = (230.0, 172.9)$ GPa). This type of composite is used for its lightweight and high overall stiffness. For the purposes of numerical experimentation, this material combination exhibits enough significant mismatch in the mechanical properties to be representative of a wide range of cases. The partitioning consisted of 512 subblocks (subdomains), each containing a random distribution of 20 nonintersecting particles occupying approximately 22% of volume. We considered external boundary loading of the form $\mathscr{E}_{ij} = 0.001$, $i, j = 1, 2, 3$:

$$\begin{bmatrix} u_1|_{\partial\Omega} \\ u_2|_{\partial\Omega} \\ u_3|_{\partial\Omega} \end{bmatrix} = \underbrace{\begin{bmatrix} \mathscr{E}_{11} & \mathscr{E}_{12} & \mathscr{E}_{13} \\ \mathscr{E}_{12} & \mathscr{E}_{22} & \mathscr{E}_{23} \\ \mathscr{E}_{31} & \mathscr{E}_{32} & \mathscr{E}_{33} \end{bmatrix}}_{\mathscr{E}} \begin{bmatrix} x_1 \\ x_2 \\ x_3 \end{bmatrix}, \tag{15}$$

which is relatively standard in micromechanical analyses. The usual motivation for such a loading is that the sample is considered so large that it experiences nearly uniform strain (linear displacements) on its boundary. For this loading, a straightforward kinematically admissible choice for $\boldsymbol{U}$ (in Box (2)) is $\boldsymbol{U} = \mathscr{E} \cdot \boldsymbol{x}$. Before we ran the full tests, we repeatedly refined the finite element mesh for several subdomains (subblocks), each containing the same number of spheres, but with different random distributions, until we obtained invariant total strain energy responses. The result was that beyond typically a $24 \times 24 \times 24$ mesh (46,875 d.o.f. per test) per subdomain, roughly 2344 d.o.f. per particle, delivered macroscopically (volumetrically averaged) mesh invariant responses. *The resulting number of total d.o.f.* (n), *if the entire domain was directly simulated with this mesh density*, *would be* $n = 21{,}567{,}171$.

Table 1 illustrates some statistics using 512 subdomains. Figs. 4–7 provide the corresponding plots of the individual responses for each subdomain. It is important to realize that since all subdomains are the same

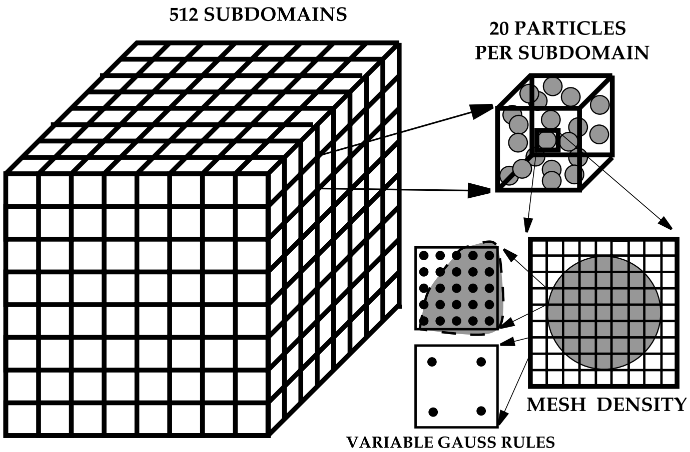

Fig. 3. A 'large' sample of aluminum with 10,240 embedded boron particles. In reality the sample is approximately 0.1 mm $\times$ 0.1 mm $\times$ 0.1 mm, while the particles are approximately 0.0035 mm in diameter.

Table 1
Results of 512 material subdomains, each containing 20 randomly distributed spheres, for a total of 10,240[a]

Subdomain quantity	Average	Standard Deviation	Max–min
W (GPa)	0.001373	7.2×10^{-6}	7.5×10^{-5}
CG-iter	48.8984	1.7737	11

[a] Note that $W \overset{\text{def}}{=} \frac{1}{|\Omega|} \int_\Omega \nabla \boldsymbol{u} : \mathbb{E} : \nabla \boldsymbol{u} \, d\Omega$.

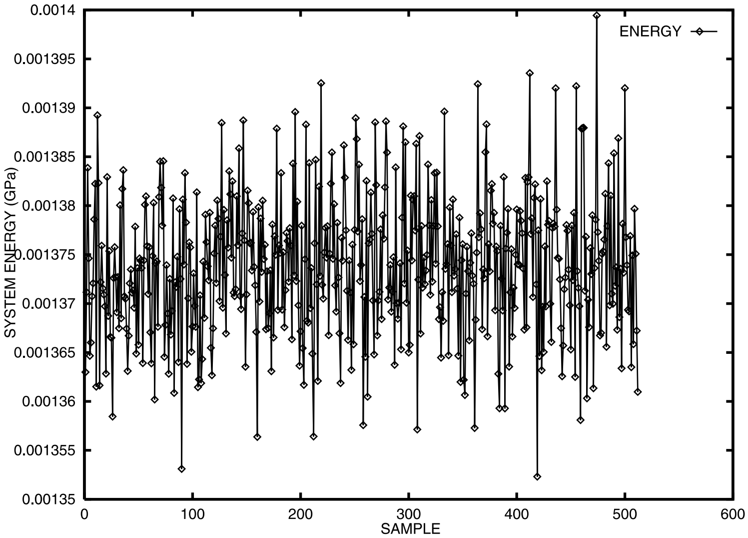

Fig. 4. 512 subdomains: the energy responses, $W \stackrel{\text{def}}{=} \frac{1}{|\Omega|}\int_{\Omega} \nabla \boldsymbol{u} : \mathbb{E} : \nabla \boldsymbol{u}\, d\Omega$ (GPa), of a block with 20 randomly distributed boron spheres embedded in an aluminum matrix.

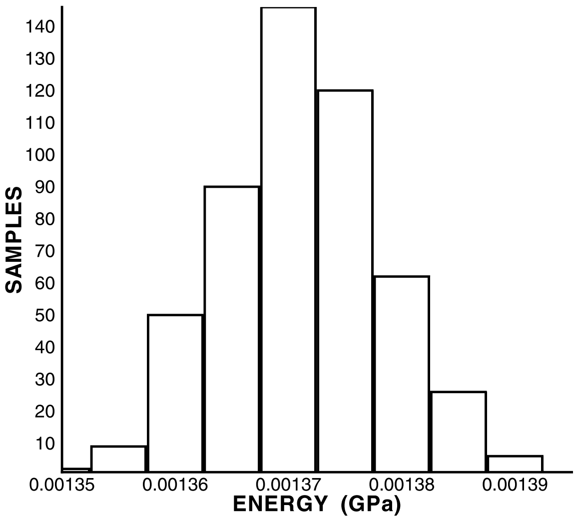

Fig. 5. 512 subdomains: the corresponding histogram for the variations in energy, $W \stackrel{\text{def}}{=} \frac{1}{|\Omega|}\int_{\Omega} \nabla \boldsymbol{u} : \mathbb{E} : \nabla \boldsymbol{u}\, d\Omega$ (GPa).

size, that the projection of $\boldsymbol{U} = \mathscr{E} \cdot \boldsymbol{x}$ on the interfacial boundaries would produce the same strain energy in each subdomain if the material had been uniform. [1] Therefore, it is logical to (statistically) compare the solution behavior between the subdomains. Throughout the tests a standard preconditioned conjugate gradient (CG) solver was used. The primary premise for its (wide) use is that a solution, to tolerable accuracy, can be achieved in much less than $O(n^3)$ operations, which is required with most Gaussian-type techniques. For overviews of a variety of such methods see [2]. The CG method, is guaranteed to converge in n iterations, provided the algebra is performed exactly. At each iteration the computational cost is $O(n^2)$ operations, and if the number of CG iterations is C, then the total cost is Cn^2 operations, where typically $C \ll n$. Use of an iterative solver allowed the use of the vector $\boldsymbol{U}$ as a starting vector to speed up the solution process. In other words, a starting vector that captures a priori the 'long wave' components (low-frequency eigenmodes) of the solution is advantageous. This increases the effectiveness of the CG

[1] Clearly, it is a homogeneous deformation in this case.

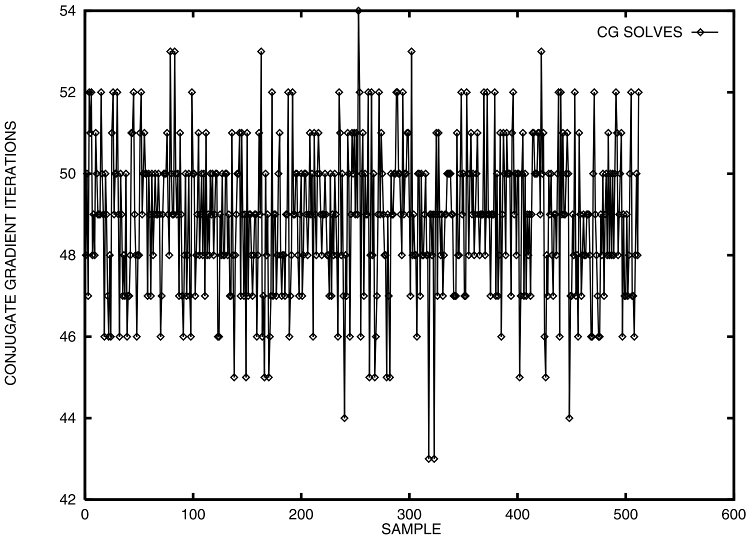

Fig. 6. 512 subdomains: the CG iterations of a block with 20 randomly distributed boron spheres embedded in an aluminum matrix.

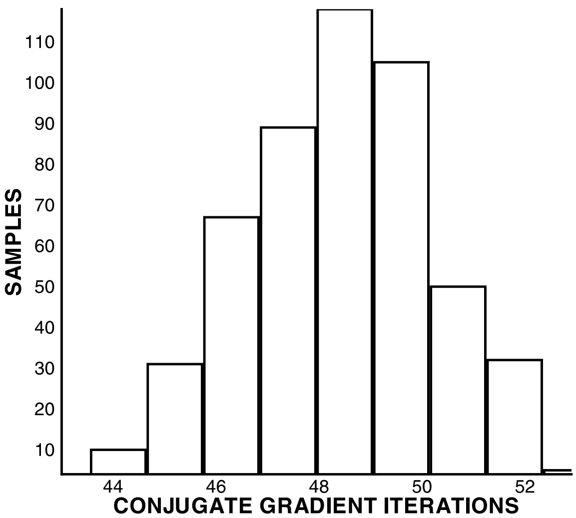

Fig. 7. 512 subdomains: the corresponding histogram for the variations in CG iterations needed for a solution.

searches for this class of problems. A well-known fact with regard to iterative solvers is the fact that they are quite adept at capturing high-frequency responses. However, they typically may require many iterations to capture 'long-wave' modes. For a discussion see [3]. For this decomposition, since the number of CG iterations to solve each subdomain problem was $m_{\mathrm{loc}} \approx 49$ (Table 1). Therefore, the cost to solve all of the subdomain problems was $m_{\mathrm{loc}}(n/N)^2 N \approx 49(n^2/512)$, as opposed to the direct cost of approximately $M_{\mathrm{glob}} n^2$, where $M_{\mathrm{glob}} > m_{\mathrm{loc}}$. In this case, the approximate cost savings are approximately direct costs/decomposed costs $\approx N M_{\mathrm{glob}}/m_{\mathrm{loc}} \geqslant 512$. The time to preprocess, solve and postprocess each 20 particle subdomain took no more than 1 min on a single RISC 6000 workstation. Clearly, the overall solution process is trivially parallelizable.

From the results of the numerical simulations, we computed the following upper bound, normalized by the energy of $\boldsymbol{U} = \mathscr{E} \cdot \boldsymbol{x}$, on the error

$$\boxed{0 \leqslant \frac{\|\boldsymbol{u} - \tilde{\boldsymbol{u}}\|^2_{E(\Omega)}}{\|\boldsymbol{U}\|^2_{E(\Omega)}} \leqslant \frac{2(\mathscr{J}(\tilde{\boldsymbol{u}}) - \mathscr{J}^-)}{\|\boldsymbol{U}\|^2_{E(\Omega)}} = 0.1073,} \tag{16}$$

where the maximized

$$\mathscr{J}^- = \frac{1}{2}\mathscr{E} : \left\langle \mathbb{E}^{-1} \right\rangle_\Omega^{-1} : \mathscr{E}|\Omega|, \qquad \mathscr{R}^* = \left\langle \mathbb{E}^{-1} \right\rangle_\Omega = \left(\frac{1}{|\Omega|} \int_\Omega \mathbb{E}^{-1}\, \mathrm{d}\Omega \right)^{-1},$$

has been used. The optimal $\mathscr{R}^*$ stems from computing

$$\frac{\partial \mathscr{J}^-}{\partial \mathscr{R}} = \mathbf{0}, \qquad \frac{\partial^2 \mathscr{J}^-}{\partial \mathscr{R}^2} < \mathbf{0} \ \Rightarrow \ \mathscr{R}^* = \left\langle \boldsymbol{E}^{-1} \right\rangle_\Omega^{-1}.$$

Remarks.

1. Under special circumstances this decomposition process can be considered as a means of statistically testing samples of heterogeneous materials. For further details see [11].
2. During the computations, to increase the resolution of the internal geometry, we applied a '2/5' Gauss rule, i.e., a $2 \times 2 \times 2$ Gauss rule if there was no material discontinuity in the element, and a $5 \times 5 \times 5$ rule if there is a material discontinuity (Fig. 3). Further details on this type of meshing procedure can be found in [11].

5. A 'total' orthogonal sum

Clearly, for the class of problems under consideration, solutions must be generated numerically, for example, as in the previous section, by the finite element method. We now consider the effect of the use of the finite element method to generate a subspatial approximation to $\tilde{\boldsymbol{u}}$, denoted $\tilde{\boldsymbol{u}}^h$, governed per subdomain by

$$\boxed{\begin{array}{l} \text{Find } \tilde{\boldsymbol{u}}_K^h \in \boldsymbol{H}_{\tilde{u}}^h(\Omega_K) \subset \boldsymbol{H}^1(\Omega),\ \tilde{\boldsymbol{u}}_K^h|_{\partial\Omega_K \cap (\Omega \cup \Gamma_u)} = \boldsymbol{U} \in \boldsymbol{H}^1(\Omega), \quad \text{such that} \\ \displaystyle\int_{\Omega_K} \nabla \boldsymbol{v}_K : \tilde{\boldsymbol{\sigma}}_K^h\, \mathrm{d}\Omega = \int_{\Omega_K} \boldsymbol{f} \cdot \boldsymbol{v}_K\, \mathrm{d}\Omega + \int_{\partial\Omega_K \cap \Gamma_t} \boldsymbol{t} \cdot \boldsymbol{v}_K\, \mathrm{d}A \\ \quad \forall \boldsymbol{v}_K^h \in \boldsymbol{H}_v^h(\Omega_K) \subset \boldsymbol{H}^1(\Omega_K), \quad \boldsymbol{v}_K^h|_{\partial\Omega_K \cap (\Omega \cup \Gamma_u)} = \mathbf{0}. \end{array}} \tag{17}$$

A critical point is that $\boldsymbol{H}_{\tilde{u}}^h(\Omega), \boldsymbol{H}_v^h(\Omega) \subset \boldsymbol{H}^1(\Omega)$. This 'inner' approximation allows the development of a straightforward decomposition. Using a subspatial approximation, by direct expansion we have

$$\begin{aligned} \mathscr{J}\left(\tilde{\boldsymbol{u}}^h\right) &= \sum_{K=1}^N \mathscr{J}_K\left(\tilde{\boldsymbol{u}}_K^h\right) \\ &= \sum_{K=1}^N \mathscr{J}_K\left(\tilde{\boldsymbol{u}}_K + \left(\tilde{\boldsymbol{u}}_K^h - \tilde{\boldsymbol{u}}_K\right)\right) \\ &= \sum_{K=1}^N \mathscr{J}_K(\tilde{\boldsymbol{u}}_K) + \sum_{K=1}^N \int_{\Omega_K} \nabla\left(\tilde{\boldsymbol{u}}_K^h - \tilde{\boldsymbol{u}}_K\right) : \mathbb{E} : \nabla \tilde{\boldsymbol{u}}_K\, \mathrm{d}\Omega \\ &\quad - \sum_{K=1}^N \int_{\Omega_K} \boldsymbol{f} \cdot \left(\tilde{\boldsymbol{u}}_K^h - \tilde{\boldsymbol{u}}_K\right) \mathrm{d}\Omega - \sum_{K=1}^N \int_{\partial\Omega_K \cap \Gamma_t} \boldsymbol{t} \cdot \left(\tilde{\boldsymbol{u}}_K^h - \tilde{\boldsymbol{u}}_K\right) \mathrm{d}A, \\ &\quad + \sum_{K=1}^N \frac{1}{2} \int_{\Omega_K} \nabla\left(\tilde{\boldsymbol{u}}_K^h - \tilde{\boldsymbol{u}}_K\right) : \mathbb{E} : \nabla\left(\tilde{\boldsymbol{u}}_K^h - \tilde{\boldsymbol{u}}_K\right) \mathrm{d}\Omega, \\ &= \sum_{K=1}^N \mathscr{J}(\tilde{\boldsymbol{u}}_K) + \sum_{K=1}^N \frac{1}{2} \int_{\Omega_K} \nabla\left(\tilde{\boldsymbol{u}}_K^h - \tilde{\boldsymbol{u}}_K\right) : \mathbb{E} : \nabla\left(\tilde{\boldsymbol{u}}_K^h - \tilde{\boldsymbol{u}}_K\right) \mathrm{d}\Omega, \end{aligned} \tag{18}$$

where, by Box (17), for $K = 1, 2, \ldots, n$

$$\int_{\Omega_K} \nabla\left(\tilde{\boldsymbol{u}}_K^h - \tilde{\boldsymbol{u}}_K\right) : \mathbb{E} : \nabla\tilde{\boldsymbol{u}}_K \, \mathrm{d}\Omega - \int_{\Omega_K} \boldsymbol{f} \cdot \left(\tilde{\boldsymbol{u}}_K^h - \tilde{\boldsymbol{u}}_K\right) \mathrm{d}\Omega - \int_{\partial\Omega_K \cap \Gamma_t} \boldsymbol{t} \cdot \left(\tilde{\boldsymbol{u}}_K^h - \tilde{\boldsymbol{u}}_K\right) \mathrm{d}A = 0. \tag{19}$$

Subtracting $\mathscr{J}(\boldsymbol{u})$ from both sides of Eq. (18) leads to

$$\mathscr{J}\left(\tilde{\boldsymbol{u}}^h\right) - \mathscr{J}(\boldsymbol{u}) = \mathscr{J}(\tilde{\boldsymbol{u}}) - \mathscr{J}(\boldsymbol{u}) + \frac{1}{2}\int_{\Omega} \nabla\left(\tilde{\boldsymbol{u}} - \tilde{\boldsymbol{u}}^h\right) : \mathbb{E} : \nabla\left(\tilde{\boldsymbol{u}} - \tilde{\boldsymbol{u}}^h\right) \mathrm{d}\Omega, \tag{20}$$

which immediately implies

$$\boxed{\left\|\boldsymbol{u} - \tilde{\boldsymbol{u}}^h\right\|_{E(\Omega)}^2 = \|\boldsymbol{u} - \tilde{\boldsymbol{u}}\|_{E(\Omega)}^2 + \left\|\tilde{\boldsymbol{u}} - \tilde{\boldsymbol{u}}^h\right\|_{E(\Omega)}^2.} \tag{21}$$

Therefore, the estimate of the error, for example, in Boxes (12) *and* (16) *implicitly contains the numerical discretization error*. Clearly, the total error is composed of two mutually orthogonal parts:

1. a partitioning error introduced by subdividing the body and applying inexact boundary data on the interfaces;
2. a numerical error, introduced by spatial discretization.

Therefore, if one has a numerical error estimator, one can isolate the pure decomposition error. Such 'filtering' processes have been performed in [11]. For details on elementary a priori numerical error estimates, see the text of Hughes [6], while for a posteriori estimates see [1].

6. Extensions and future work

In order to achieve further reduction of the global/local error, the subdomain interfacial boundary conditions must be improved. Clearly, the error bound in Box (12), and the orthogonality expression in Box (21) still hold, provided that the modified, hopefully improved, local boundary data deliver a globally kinematically admissible solution. Thus, we now discuss a few methods which consist of updating the numerical d.o.f. on the interfaces of a finite element discretization. Without loss of generality, and for simplicity of presentation, we consider that we have meshed each subdomain in the substructuring process so that a global nodally conforming trilinear hexahedral finite element mesh results.

6.1. Method I: global/local CG iterations

One can consider a process of updating interfacial nodal values as having as its goal the minimization of the discrete analog of $\mathscr{J}(\tilde{\boldsymbol{u}})$, namely $\mathscr{J}(\tilde{\boldsymbol{u}}^h)$, which is convex in terms of the finite element nodal displacements. There exist a variety of classical techniques which could drive a process to minimize potential energies, the most applicable in the linearly elastic case being the CG method, which, for the sake of completeness, we briefly discuss in the context of a global/local strategy.

Suppose we wish to solve the discrete system $[\boldsymbol{K}]\{\boldsymbol{u}^h\} = [\boldsymbol{B}]$. $[\boldsymbol{K}]$ is a symmetric positive definite $n \times n$ matrix, $\{\boldsymbol{u}^h\}$ is the $n \times 1$ solution vector, $[\boldsymbol{B}]$ is the $n \times 1$ right-hand side, and n is the number of discrete unknowns. We define a discrete potential

$$\Pi \stackrel{\mathrm{def}}{=} \frac{1}{2}\left\{\boldsymbol{u}^h\right\}^{\mathrm{T}}[\boldsymbol{K}]\left\{\boldsymbol{u}^h\right\} - \left\{\boldsymbol{u}^h\right\}^{\mathrm{T}}[\boldsymbol{B}].$$

Correspondingly, from basic calculus we have

$$\nabla\Pi \stackrel{\mathrm{def}}{=} \left\{\frac{\partial\Pi}{\partial u_1}, \frac{\partial\Pi}{\partial u_2}, \ldots, \frac{\partial\Pi}{\partial u_n}\right\}^{\mathrm{T}} = \boldsymbol{0} \;\Rightarrow\; [\boldsymbol{K}]\left\{\boldsymbol{u}^h\right\} - [\boldsymbol{B}] = \boldsymbol{0}.$$

Therefore, the minimizer of the potential Π is also the solution to the discrete system. The CG method is based upon minimizing Π by successively updating a starting vector. Therefore, the substructuring method described in this work can be considered as a construction of an advanced initial starting guess, $\tilde{\boldsymbol{u}}^h$, to the solution of the global problem formed by directly discretizing the entire body with no decomposition. If we are to directly apply the CG method, one will reduce $\mathscr{J}(\tilde{\boldsymbol{u}}^h)$, to the minimum value for the corresponding global mesh discretization. Since a CG approach updates all values in the entire domain simultaneously, via a global matrix–vector multiply, each iteration can be thought of as providing global transfer of information, i.e., microstructural corrections to the initial solution $\tilde{\boldsymbol{u}}^h$, and thus the interfacial boundary conditions. The minimum of the discrete potential is the global solution for the given finite element discretization. However, instead of a direct application of the CG method, one can perform a set number of global CG iterations, $M_{\rm glob}$, then reevaluate the local boundary value problems with the new local boundary data. Per subdomain we have $m_{\rm loc}(n/N)^2$ operation counts, where $m_{\rm loc}$ is the number of local CG iterations for subdomain solution convergence. For simplicity, we have assumed that one would use the CG method to solve each subdomain problem, and that $m_{\rm loc}$ is approximately the same for each subdomain. Therefore, for N total subdomains we have $m_{\rm loc}(n/N)^2N$ operation counts. Let us denote the number of times that we globally iterate and resolve the local problems as, $\mathscr{S}$. Thus, in total, we have

$$\mathscr{S}\left(M_{\rm glob}n^2 + Nm_{\rm loc}\left(\frac{n}{N}\right)^2\right) = \mathscr{S}\left(M_{\rm glob} + \frac{m_{\rm loc}}{N}\right)n^2.$$

Therefore, a direct CG approach and a projecting global/local resolve approach compare as follows:

$$\boxed{\underbrace{\hat{C}n^2 \stackrel{\rm def}{=} \mathscr{S}\left(M_{\rm glob} + \frac{m_{\rm loc}}{N}\right)n^2}_{\text{projecting and resolving}} \quad \text{and} \quad \underbrace{Cn^2}_{\text{conjugate gradient}}.} \tag{22}$$

Clearly, the magnitudes of $\hat{C}$ and C determine the relative performance of the two methods.

6.2. Method II: iterative equilibration

Clearly, when decomposing the structure by a projection of a kinematically admissible function onto the partitioning interfaces, regardless of the constitutive law, the error is due to the jumps in tractions at the interfaces (Box (4)). If the interfaces would be in equilibrium, then there would be no traction jumps. Therefore, an approach which attempts to eliminate the jumps in tractions is sought next.

6.2.1. Global equilibration

For global equilibration one treats the entire interface as a single subdomain, denoted $\omega \subset \Omega$, and solves the following (Fig. 8):

$$\boxed{\begin{array}{l}\text{Find } \boldsymbol{s} \in \boldsymbol{H}^1(\omega),\ \ \boldsymbol{s}|_{\partial\omega\cap(\omega\cup\Gamma_u)} = \tilde{\boldsymbol{u}} \in \boldsymbol{H}^1(\Omega), \quad \text{such that}\\ \displaystyle\int_\omega \nabla\boldsymbol{v} : \boldsymbol{\sigma}(\boldsymbol{s})\,\mathrm{d}\omega = \int_\omega \boldsymbol{f}\cdot\boldsymbol{v}\,\mathrm{d}\omega + \int_{\partial\omega\cap\Gamma_t} \boldsymbol{t}\cdot\boldsymbol{v}\,\mathrm{d}a\\ \quad\forall\boldsymbol{v} \in \boldsymbol{H}^1(\omega),\ \ \boldsymbol{v}|_{\partial\omega\cap(\omega\cup\Gamma_u)} = \boldsymbol{0}.\end{array}} \tag{23}$$

The new interfacial displacements are then computed, and the subdomain problems are re-solved. The process is repeated until convergence. The entire interface problem can be quite large. A less expensive approach, amenable to trivial parallel processing, follows.

6.2.2. Local (nodal) equilibration

For local equilibration, one prescribes small nonintersecting 'nodal domains', ω_K (Fig. 8), surrounding each interfacial node $1 \leqslant K \leqslant M$ (M = number of interfacial nodes):

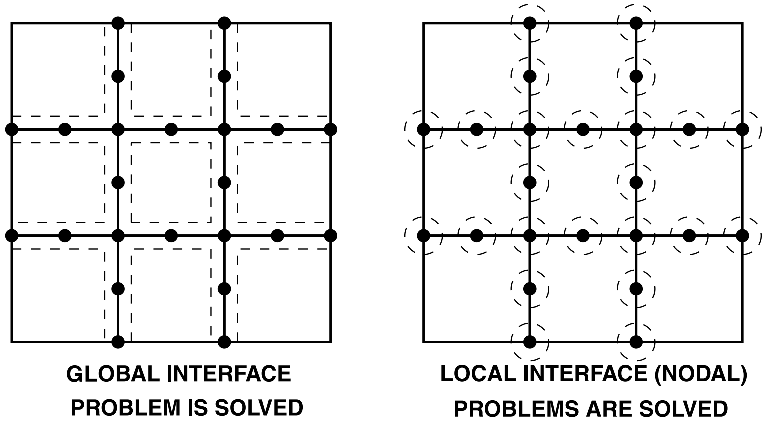

Fig. 8. Global equilibration and local equilibration.

$$\boxed{\begin{array}{l} \text{Find } \boldsymbol{s}_K \in \boldsymbol{H}^1(\omega_K),\ \ \boldsymbol{s}_K|_{\partial\omega_K\cap(\omega_K\cup\Gamma_u)} = \tilde{\boldsymbol{u}} \in \boldsymbol{H}^1(\Omega), \quad \text{such that} \\ \displaystyle\int_{\omega_K} \nabla \boldsymbol{v}_K : \boldsymbol{\sigma}_K(\boldsymbol{s})\, \mathrm{d}\omega_K = \int_{\omega_K} \boldsymbol{f}\cdot\boldsymbol{v}_K\, \mathrm{d}\omega_K + \int_{\partial\omega_K\cap\Gamma_t} \boldsymbol{t}\cdot\boldsymbol{v}_K\, \mathrm{d}a_K \\ \quad \forall \boldsymbol{v}_K \in \boldsymbol{H}^1(\omega_K),\ \ \boldsymbol{v}_K|_{\partial\omega_K\cap(\omega_K\cup\Gamma_u)} = \boldsymbol{0}. \end{array}} \tag{24}$$

The new interfacial displacements are then computed, and the subdomain problems are resolved. The process is repeated until convergence. The advantage of such an approach is that the nodal domains can be processed independently of one another. The disadvantage is that global equilibrium is not satisfied throughout the entire interface. Either of the introduced approaches can be considered as a fixed-point iteration, which we discuss next.

6.2.3. General fixed-point iterations

Consider a general system of coupled partial differential equations given by $\mathscr{A}(\boldsymbol{s}) = \mathscr{F}$, where $\boldsymbol{s}$ is a solution, and where it is assumed that the operator, $\mathscr{A}$, is invertible. One desires that the sequence of iterated solutions, $\boldsymbol{s}^I, I = 1, 2, \ldots,$ converge to $\mathscr{A}^{-1}(\mathscr{F})$ as $I \to \infty$. If $\boldsymbol{s}^I$ is a function of $\mathscr{A}, \mathscr{F}, \boldsymbol{s}^I, \ldots, \boldsymbol{s}^{I-K}$ one says that K is the order of iteration. It is assumed that the Ith iterate can be represented by some arbitrary function $\boldsymbol{s}^I = \mathscr{T}^I(\mathscr{A}, \mathscr{F}, \boldsymbol{s}^{I-1})$. One makes the following split $\boldsymbol{s}^I = \mathscr{G}^I(\boldsymbol{s}^{I-1}) + \boldsymbol{r}^I$. For this method to be useful the exact solution should be reproduced. In other words, when $\boldsymbol{s} = \mathscr{A}^{-1}(\mathscr{F})$, then $\boldsymbol{s} = \mathscr{A}^{-1}(\mathscr{F}) = \mathscr{G}^I(\mathscr{A}^{-1}(\mathscr{F})) + \boldsymbol{r}^I$. Therefore, one has the following consistency condition $\boldsymbol{r}^I = \mathscr{A}^{-1}(\mathscr{F}) - \mathscr{G}^I(\mathscr{A}^{-1}(\mathscr{F}))$, and as a consequence, $\boldsymbol{s}^I = \mathscr{G}^I(\boldsymbol{s}^{I-1}) + \mathscr{A}^{-1}(\mathscr{F}) - \mathscr{G}^I(\mathscr{A}^{-1}(\mathscr{F}))$. Convergence of the iteration can be studied by defining the error vector:

$$\begin{aligned} \boldsymbol{e}^I &= \boldsymbol{s}^I - \boldsymbol{s} \\ &= \boldsymbol{s}^I - \mathscr{A}^{-1}(\mathscr{F}) \\ &= \mathscr{G}^I\left(\boldsymbol{s}^{I-1}\right) + \mathscr{A}^{-1}(\mathscr{F}) - \mathscr{G}^I\left(\mathscr{A}^{-1}(\mathscr{F})\right) - \mathscr{A}^{-1}(\mathscr{F}) \\ &= \mathscr{G}^I\left(\boldsymbol{s}^{I-1}\right) - \mathscr{G}^I\left(\mathscr{A}^{-1}(\mathscr{F})\right). \end{aligned} \tag{25}$$

One sees that, if $\mathscr{G}^I$ is linear and invertible, the above reduces to $\boldsymbol{e}^I = \mathscr{G}^I(\boldsymbol{s}^{I-1} - \mathscr{A}^{-1}(\mathscr{F})) = \mathscr{G}^I(\boldsymbol{e}^{I-1})$. Therefore, if the spectral radius of $\mathscr{G}^I$, i.e., the magnitude of its largest eigenvalue, is less than unity for each iteration I, then $\boldsymbol{e}^I \to \boldsymbol{0}$ for any arbitrary starting solution $\boldsymbol{s}^{I=0}$ as $I \to \infty$.

6.2.4. An example

Again consider the simple one-dimensional structure

$$0 < x < L: \ \frac{\mathrm{d}}{\mathrm{d}x}\left(E(x)\frac{\mathrm{d}u}{\mathrm{d}x}\right) = 0, \quad u(0) = \Delta_0,\ \ u(L) = \Delta_L,$$

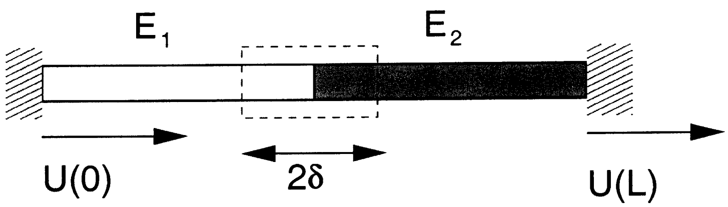

Fig. 9. A one-dimensional equilibration example.

in Fig. 9. Consider two subdomains, and one interfacial problem, which are solved in an iterative manner $i = 1, 2, \ldots, N$, until

$$\left|e^I\left(\frac{L}{2}\right)\right| = \left|s^I\left(\frac{L}{2}\right) - u\left(\frac{L}{2}\right)\right| \leqslant \text{tol},$$

$$\boxed{\begin{array}{l}
\text{subdomain\#1} \quad \left(0 < x < \frac{L}{2}\right) : \ \frac{\mathrm{d}}{\mathrm{d}x}\left(E_1 \frac{\mathrm{d}\tilde{u}_1^I}{\mathrm{d}x}\right) = 0, \quad \tilde{u}_1^I(0) = \Delta_0 \ \tilde{u}_1^I\left(\frac{L}{2}\right) = s^I\left(\frac{L}{2}\right), \\
\text{subdomain\#2} \quad \left(\frac{L}{2} < x < L\right) : \ \frac{\mathrm{d}}{\mathrm{d}x}\left(E_2 \frac{\mathrm{d}\tilde{u}_2^I}{\mathrm{d}x}\right) = 0, \quad \tilde{u}_2^I\left(\frac{L}{2}\right) = s^I\left(\frac{L}{2}\right), \ \tilde{u}_2^I(L) = \Delta_L, \\
\text{interface} \quad \left(\frac{L}{2} - \delta < x < \frac{L}{2} + \delta\right) : \ \frac{\mathrm{d}}{\mathrm{d}x}\left(E(x) \frac{\mathrm{d}s^I}{\mathrm{d}x}\right) = 0, \\
\quad s^I\left(\frac{L}{2} - \delta\right) = \tilde{u}_1^I\left(\frac{L}{2} - \delta\right), \quad s^I\left(\frac{L}{2} + \delta\right) = \tilde{u}_2^I\left(\frac{L}{2} + \delta\right).
\end{array}} \tag{26}$$

Since there is only a single one-dimensional interface, the global and local equilibration methods are the same. A simple starting value, that of the regularized solution,

$$s^0\left(\frac{L}{2}\right) = \frac{u(L) + u(0)}{2}$$

is chosen. After some algebra we have, $\mathscr{G} = 1 - \Theta$, where $\Theta = 2\delta/L$, yielding

$$\boxed{\begin{aligned}
s^I\left(\frac{L}{2}\right) &= \underbrace{(1 - \Theta)}_{\mathscr{G}} s^{I-1}\left(\frac{L}{2}\right) + \underbrace{\Theta\left(\left(\frac{E_2}{E_1 + E_2}\right)(u(L) - u(0)) + u(0)\right)}_{r}, \\
e^I\left(\frac{L}{2}\right) &= s^I\left(\frac{L}{2}\right) - u\left(\frac{L}{2}\right) \\
&= (1 - \Theta)\left(s^{I-1}\left(\frac{L}{2}\right) - u\left(\frac{L}{2}\right)\right) \\
&= (1 - \Theta) e^{I-1}\left(\frac{L}{2}\right) \\
&= (1 - \Theta)^I e^{I=0}\left(\frac{L}{2}\right).
\end{aligned}} \tag{27}$$

One sees that convergence occurs if $(1 - \Theta) < 1$, which implies $\delta > 0$. The rate of convergence is linear and is controlled by the size of δ.

To illustrate the approach we compared it to classical a classical overlapping Schwarz method (see [7]), which for this simple structure could be written as

$$\boxed{\begin{array}{ll} \text{subdomain\#1} \quad \left(0 < x < \dfrac{L}{2} + \delta\right): \ \dfrac{\mathrm{d}}{\mathrm{d}x}\left(E\dfrac{\mathrm{d}\tilde{u}_1^I}{\mathrm{d}x}\right) = 0, \quad \tilde{u}^I(0) = \Delta_0, \quad \tilde{u}_1^I\left(\dfrac{L}{2} + \delta\right) = \tilde{u}_2^{I-1}\left(\dfrac{L}{2} + \delta\right), \\ \text{subdomain\#2} \quad \left(\dfrac{L}{2} - \delta < x < L\right): \ \dfrac{\mathrm{d}}{\mathrm{d}x}\left(E\dfrac{\mathrm{d}\tilde{u}_2^I}{\mathrm{d}x}\right) = 0, \quad \tilde{u}_2^I\left(\dfrac{L}{2} - \delta\right) = \tilde{u}_1^I\left(\dfrac{L}{2} - \delta\right), \quad \tilde{u}_2^I(L) = \Delta_L. \end{array}} \tag{28}$$

Depicted in Figs. 10–12 are the relative performances of both approaches (equilibration and overlapping Schwarz). The parameters were $L = 1$, $E_1 = 10 \times 10^9$ GPa, $E_2 = 100 \times 10^9$ GPa. Each of the approaches

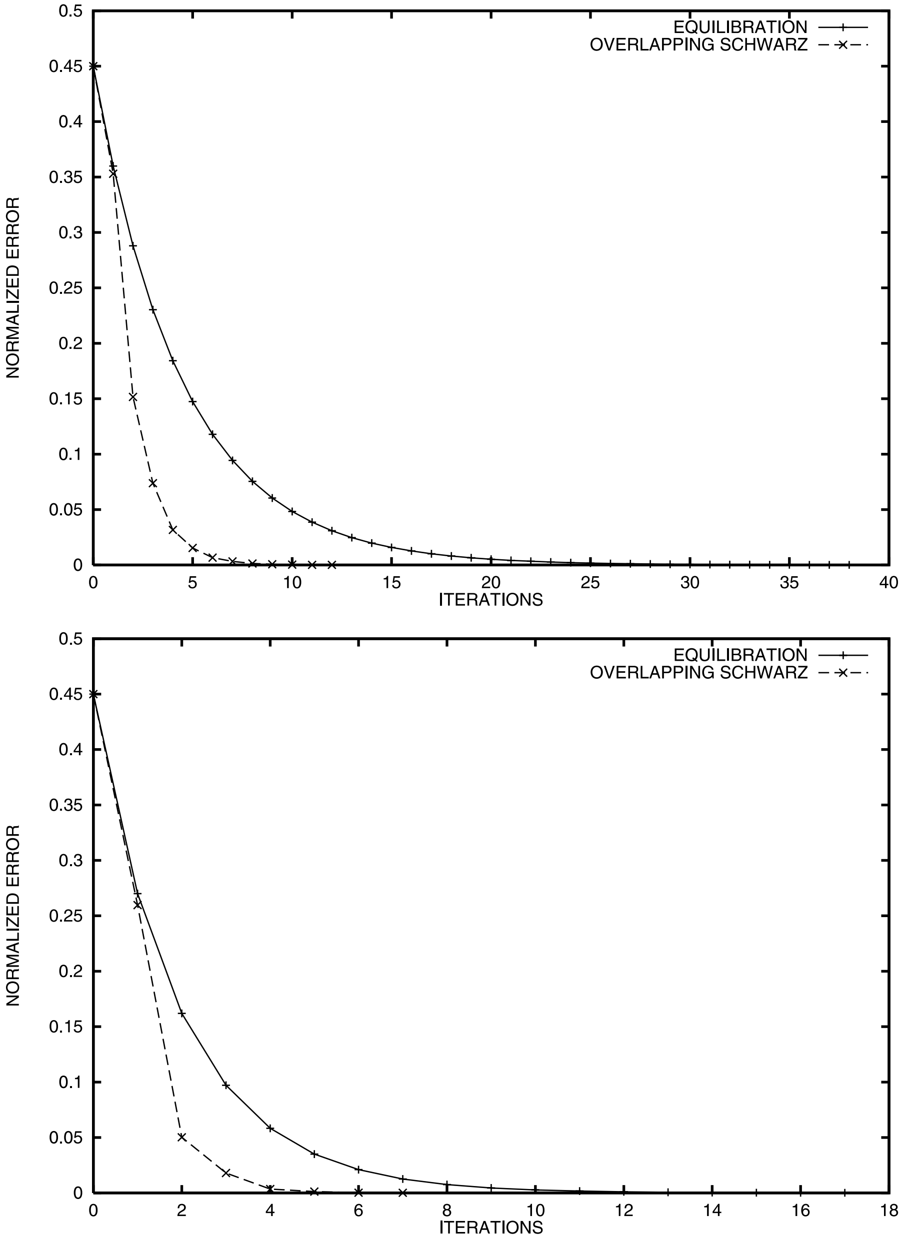

Fig. 10. Normalized error $\stackrel{\text{def}}{=} \left|\frac{\tilde{u}(L/2) - u(L/2)}{u(L/2)}\right|$. *Top* for an overlap of $\delta = 0.1$ and *bottom* for $\delta = 0.2$.

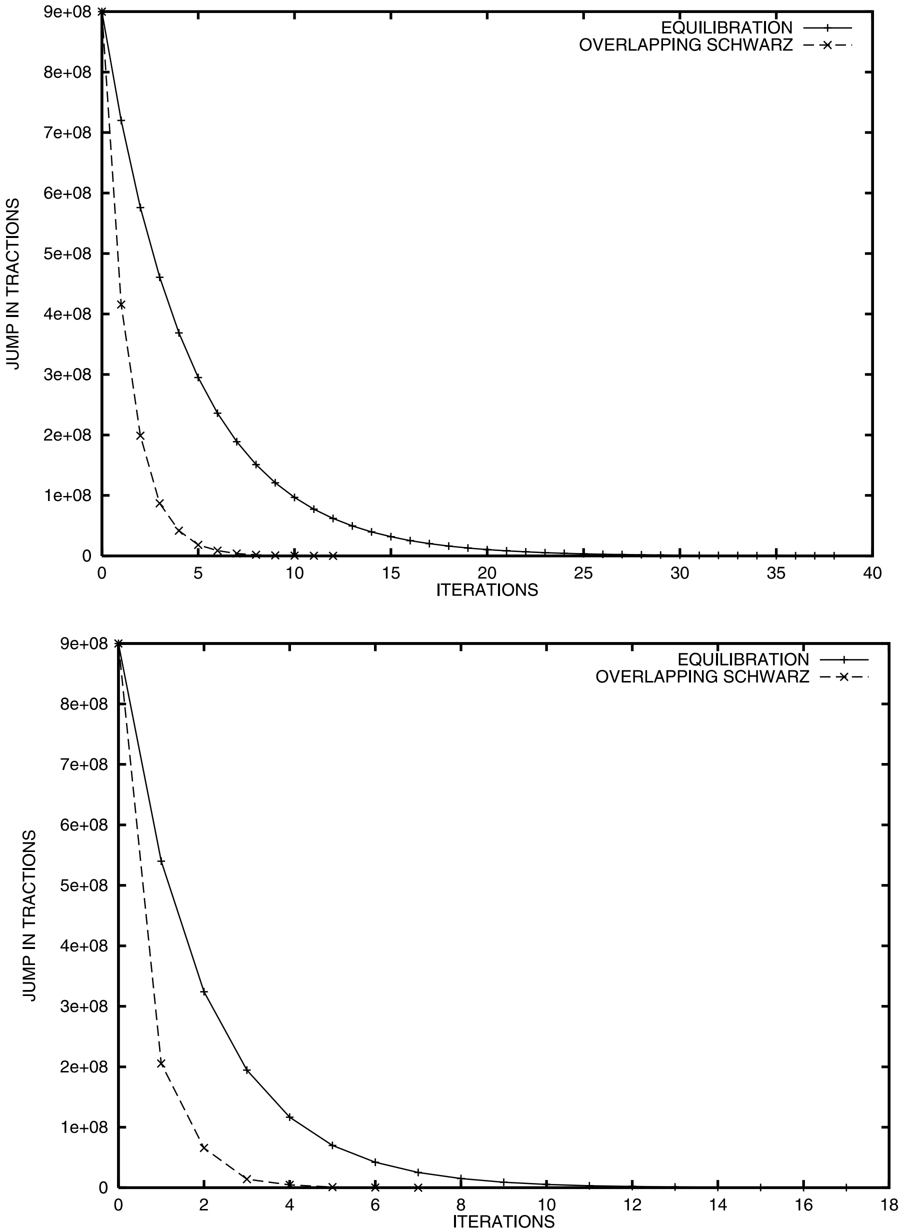

Fig. 11. Jump in tractions $\stackrel{\text{def}}{=} \left|E_1 \frac{\mathrm{d}\tilde{u}_1(L/2)}{\mathrm{d}x} - E_2 \frac{\mathrm{d}\tilde{u}_2(L/2)}{\mathrm{d}x}\right|$. *Top* for an overlap of $\delta = 0.1$ and *bottom* for $\delta = 0.2$.

iteratively improved the interfacial data by balancing the jumps in the tractions via information exchange between subdomains. Clearly, the overlapping Schwarz method attained a faster rate of convergence since more information is provided via the fact that the entire extended subdomain problem is solved during the iterative process. Generally, the local equilibration method is less expensive to compute for three-dimensional problems, however, as illustrated by the preceding one-dimensional example, it will probably exhibit slower rates of convergence.

6.3. Concluding remarks

Depending on the problem, one method may exhibit superiority over another in terms of the overall cost for a desired solution accuracy. It is important to remark that, in the general three-dimensional case, for

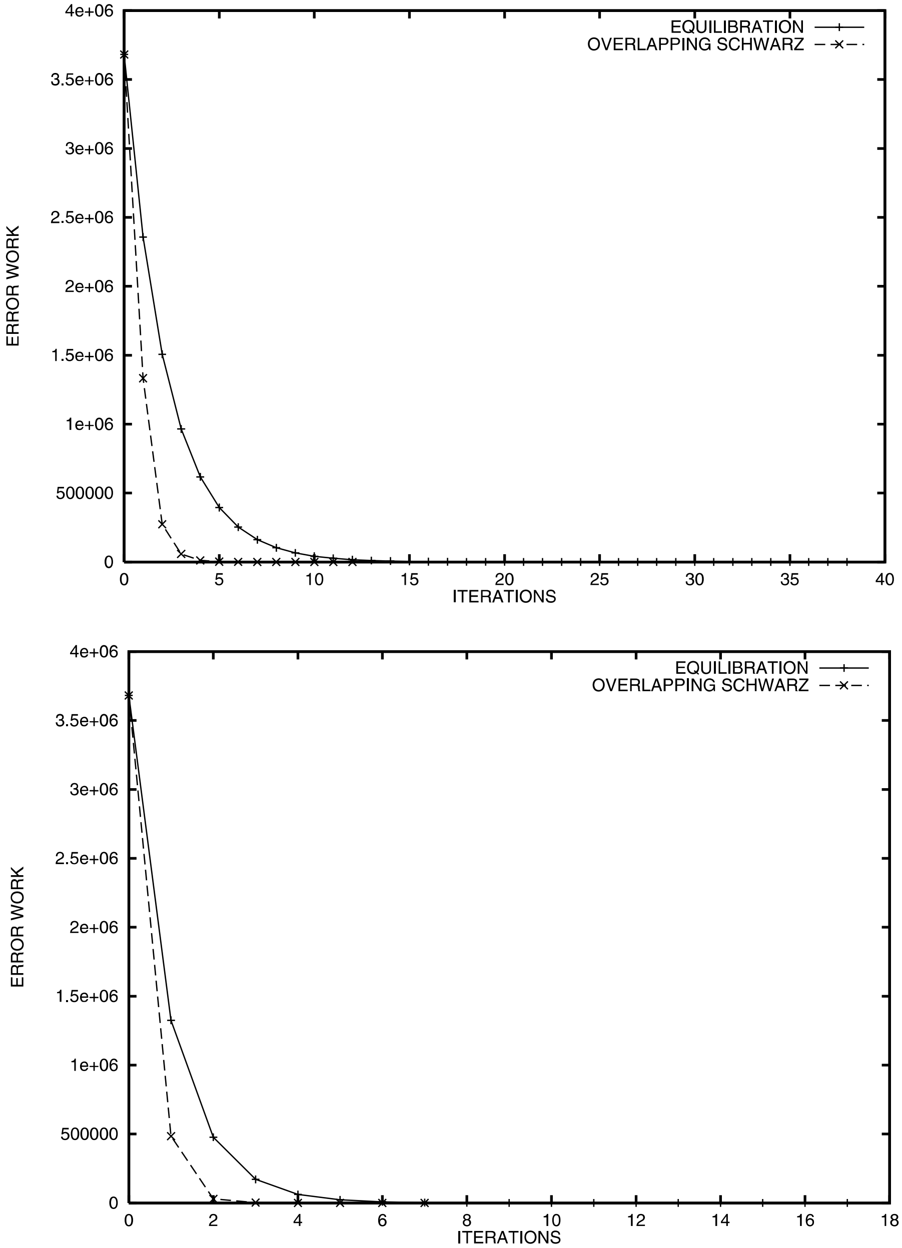

Fig. 12. Error work $\stackrel{\mathrm{def}}{=} \left|\left(E_1 \frac{\mathrm{d}\tilde{u}_1(L/2)}{\mathrm{d}x} - E_2 \frac{\mathrm{d}\tilde{u}_2(L/2)}{\mathrm{d}x}\right)\left(u\left(\frac{L}{2}\right) - \tilde{u}\left(\frac{L}{2}\right)\right)\right|$. *Top* for an overlap of $\delta = 0.1$ and *bottom* for $\delta = 0.2$.

either the global/local CG approach or the iterative equilibration approach, one can determine whether the solution is improving by monitoring the potential of each iterate, $\mathscr{J}(\tilde{\boldsymbol{u}}^I)$. A decreasing potential indicates that the solution is improving since $\|\boldsymbol{u} - \tilde{\boldsymbol{u}}^I\|^2_{E(\Omega)} = 2(\mathscr{J}(\tilde{\boldsymbol{u}}^I) - \mathscr{J}(\boldsymbol{u}))$ and $\mathscr{J}(\boldsymbol{u})$ is fixed. Clearly, the error bound in Box (12) holds for the iteratively generated kinematically admissible solutions, and is

$$\boxed{\begin{aligned} &\left\|\boldsymbol{u} - \tilde{\boldsymbol{u}}^I\right\|^2_{E(\Omega)} = 2\Big(\mathscr{J}(\tilde{\boldsymbol{u}}^I) - \mathscr{J}(\boldsymbol{u})\Big) \leqslant 2\Big(\mathscr{J}(\tilde{\boldsymbol{u}}^I) - \mathscr{J}^-\Big), \\ &\mathscr{J}^- = \mathscr{J}\left(\boldsymbol{u}^{\mathrm{R}}\right) - \frac{1}{2}\underbrace{\int_\Omega \left((\mathscr{R} - \mathbb{E}) : \nabla \boldsymbol{u}^{\mathrm{R}}\right) : \ \mathbb{E}^{-1} : \ \left((\mathscr{R} - \mathbb{E}) : \ \nabla \boldsymbol{u}^{\mathrm{R}}\right) \mathrm{d}\Omega}_{=(\mathscr{H}^+)^2}. \end{aligned}} \tag{29}$$

Thus, one should maximize $\mathscr{J}^{-}$ over $\boldsymbol{u}^{\mathrm{R}}$, via $\mathscr{R}$, and retain it for any subsequent iterations, since it is iteration independent. As we have indicated earlier, the only approximation in this entire estimate is $\|\boldsymbol{u}-\boldsymbol{u}^{\mathrm{R}}\|_{E(\Omega)} \leqslant \mathscr{H}^{+}$, *which is exact for the previous one-dimensional example, using the regularized parameter*

$$\mathsf{R} = \left(\frac{1}{L}\int_0^L \frac{1}{E}\,\mathrm{d}x\right)^{-1}.$$

Application of the global/local CG approach, iterative equilibration or classical overlapping methods to three-dimensional problems is under current investigation.

References

[1] M. Ainsworth, J.T. Oden, A Posteriori Error Estimation in Finite Element Analysis, Wiley, New York, 2000.
[2] O. Axelsson, Iterative Solution Methods, Cambridge University Press, Cambridge, 1994.
[3] W. Briggs, A multigrid tutorial, 1997, SIAM Issue.
[4] C. Huet, Application of variational concepts to size effects in elastic heterogeneous bodies, J. Mech. Phys. Solids 38 (1990) 813–841.
[5] C. Huet, Hierarchies and bounds for size effects in heterogeneous bodies, in: G.A. Maugin (Ed.), Continuum Models and Discrete Systems, vol. 2, 1991, pp. 127–134.
[6] T.J. Hughes, The Finite Element Method, Prentice- Hall, Englewood Cliffs, NJ, 1989.
[7] P. Le Tallec, Domain decomposition methods in computational mechanics, Comput. Mech. Adv. 1 (1994) 121–220.
[8] J.T. Oden, T.I. Zohdi, Analysis and adaptive modeling of highly heterogeneous elastic structures, Comput. Methods Appl. Mech. Engrg. 148 (1997) 367–391.
[9] T.I. Zohdi, J.T. Oden, G.J. Rodin, Hierarchical modeling of heterogeneous bodies, Comput. Methods Appl. Mech. Engrg. 138 (1996) 273–298.
[10] T.I. Zohdi, P. Wriggers, A domain decomposition method for bodies with microstructure based upon material regularization, Int. J. Solids Struct. 36 (17) (1999) 2507–2526.
[11] T.I. Zohdi, P. Wriggers, Some aspects of the computational testing of the mechanical properties of microheterogeneous material samples, Int. J. Numer. Methods Engrg. 50 (2001) 2573–2599.
[12] T.I. Zohdi, Overall solution-difference bounds on the effects of material inhomogeneities, J. Elasticity 58 (3) (2001) 249–255.